

# 1-Million Droplet Array with Wide-Field Fluorescence Imaging for Digital PCR

Andrew C. Hatch,<sup>a</sup> Jeffrey S. Fisher,<sup>a</sup> Armando R. Tovar,<sup>a</sup> Albert T. Hsieh,<sup>a</sup> Robert Lin,<sup>a</sup> Stephen L. Pentoney,<sup>b</sup> David L. Yang,<sup>b</sup> and Abraham P. Lee\*<sup>a</sup>

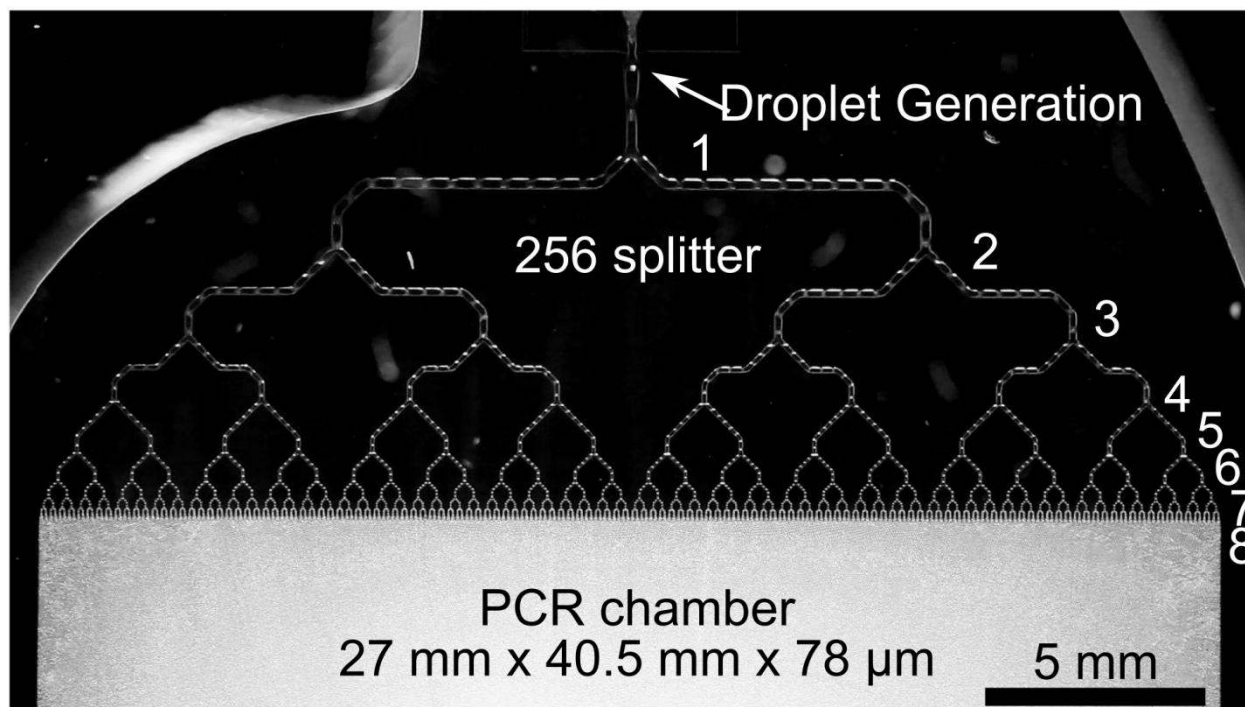
<sup>a</sup> Department of Biomedical Engineering, University of California-Irvine, 3120 Natural Sciences II Irvine, CA 92697, USA. Fax: 949-824-1727; Tel: 949-824-9691; E-mail: aplee@uci.edu

<sup>b</sup> Beckman Coulter, Inc., 250 S. Kraemer Blvd., Brea, CA 92821, USA. Fax: 714-961-3971; Tel: 714-961-3112; E-mail: dlyang@beckman.com

## Electronic Supplementary Information

### 1. Droplet Generation

High throughput droplet generation was achieved using a 256 droplet splitter to generate 1-million droplets with 50-66% water/oil (w/o) volume ratios in 2-7 minutes at flow rates of 8-25  $\mu\text{L}/\text{min}$  PCR solution and 4-25  $\mu\text{L}/\text{min}$  oil respectively. Video S1 shows droplet generation at a slower generation rate of 4  $\mu\text{L}/\text{min}$  aqueous solution and 2  $\mu\text{L}/\text{min}$  oil for video capture at 30 fps.



**Video S1:** 256 droplet splitter device and filling of large droplet array chamber. A 13 nL parent droplet is formed at a flow-focusing junction then passes through 8 bifurcation junctions to form 256 daughter droplets at a rate of 2-8.3 kHz. Video captured on a Canon 5D Mark II dSLR camera at 30 fps. Scale bar 5 mm.

## 2. Macro Lens f-number and Numerical Aperture

Traditional camera lenses are described in terms of f/number,  $f/\#$ , rather than numerical aperture, NA, which are commonly used to describe microscope objectives.  $F/\#$  can be related to NA using the approximation described in eqn (2)<sup>1</sup>.

$$f/\# \approx 1/2NA \quad (1)$$

At high magnification values, the working f-number,  $f/\#_w$ , is used instead, and describes the approximate light gathering ability of the lens based on the approximation described in eqn (2)<sup>1</sup>.



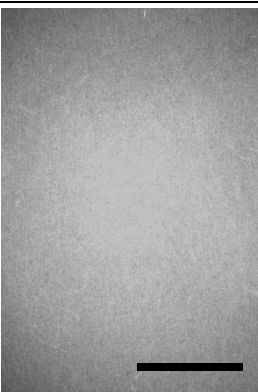
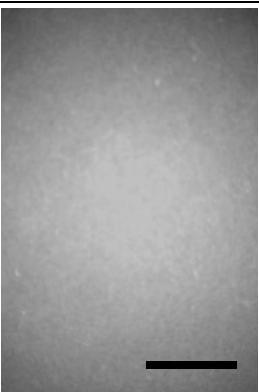


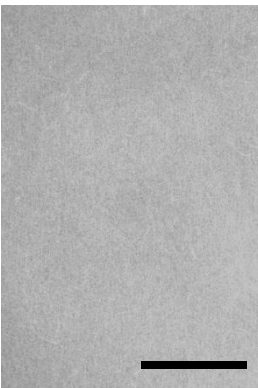
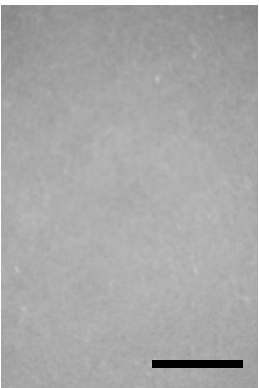
$$f/\#_w \approx (1 + m)f/\# \quad (2)$$

where  $m$  is the absolute value of magnification expressed as a positive number. The 100mm Macro lens is able to achieve 1x magnification and has a rated  $f/\#$  of  $f/2.8$ , which substitution of  $f/2.8$  and  $m=1$  into eqn (2) yields an  $f/\#_w$  of  $\sim 5.6$ . This number can then be used to estimate numerical aperture, using equation 1 to yield  $NA = \sim 0.089$ . At lower magnifications this values approaches the theoretical maximum  $f/2.8$  which corresponds to  $\sim NA = 0.175$ .

### 3. Uniformity of imaging setup

Imaging uniformity of the camera/lens is evaluated by itself and compared with the addition of the 32mm emission and the excitation illumination source described in Figure 2 of the manuscript. Table S1 shows grayscale images of white paper in four different scenarios to compare uniformity of the lens, filter, excitation lightsource, and magnification and the improvement using the camera's built-in peripheral illumination correction ability. The filter causes a fairly large reduction in light uniformity with the fluorescence excitation source reducing the intensity a little further.

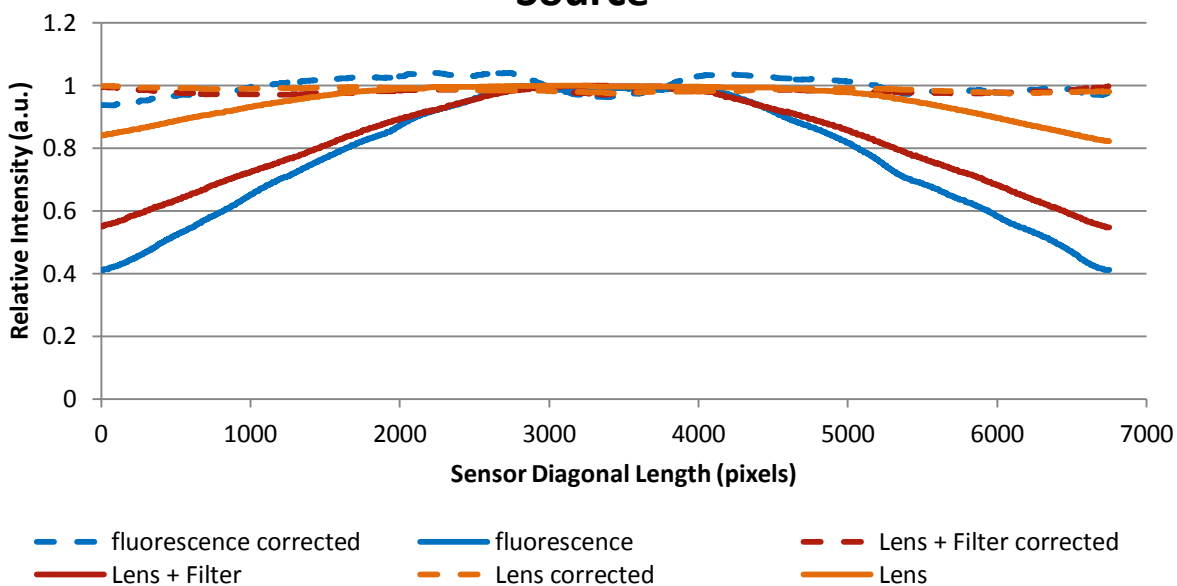
**Table S1:** Image uniformity before and after peripheral correction

Image	Lens	Lens + filter	Fluorescence 1x magnification	Fluorescence 0.85x magnification
<b>Original Image</b>				
<b>After Peripheral Correction</b>				

Images were captured on the dSLR camera with 100mm Macro lens captured at  $f/2.8$  aperture to demonstrate the performance of the lens only, the lens combined with filter, and fluorescence images using excitation light source at both 1x and 0.85x magnification (scale bars 1 cm)

Figure S1 shows diagonal line profile plots of the image intensity across the sensor for the 1x magnification images shown Table S1. The 32 mm lens causes a noticeable decrease in imaging uniformity with the excitation light source reducing it further still. After applying peripheral illumination correction the intensity is much more uniform across the picture frame. Figure S2 shows how the aperture setting or  $f/\#$  of the lens can be adjusted improve uniformity but this requires longer exposure times and may also reduce imaging contrast due to more light refraction with a smaller aperture. Figure S3 shows the change in uniformity when using a 1x magnification and a 0.85x magnification. Using a larger diameter filter would provide the best advantage but will also increase working angles causing concern for interference filters as discussed later on. A peripheral illumination correction helps significantly improve imaging uniformity in the digital domain.

## Uniformity of Lens, Filter, and Illumination Source



**Figure S1:** Imaging uniformity of dSLR camera using  $f/2.8$  aperture at 1x magnification with uniform Brightfield illumination of lens by itself (orange), Brightfield illumination with lens + filter (red), and fluorescence intensity using lens + filter + excitation illumination source. Solid lines are the original intensity profiles and dashed lines are intensity profiles after peripheral illumination correction.

## Image uniformity vs. $f/\#$

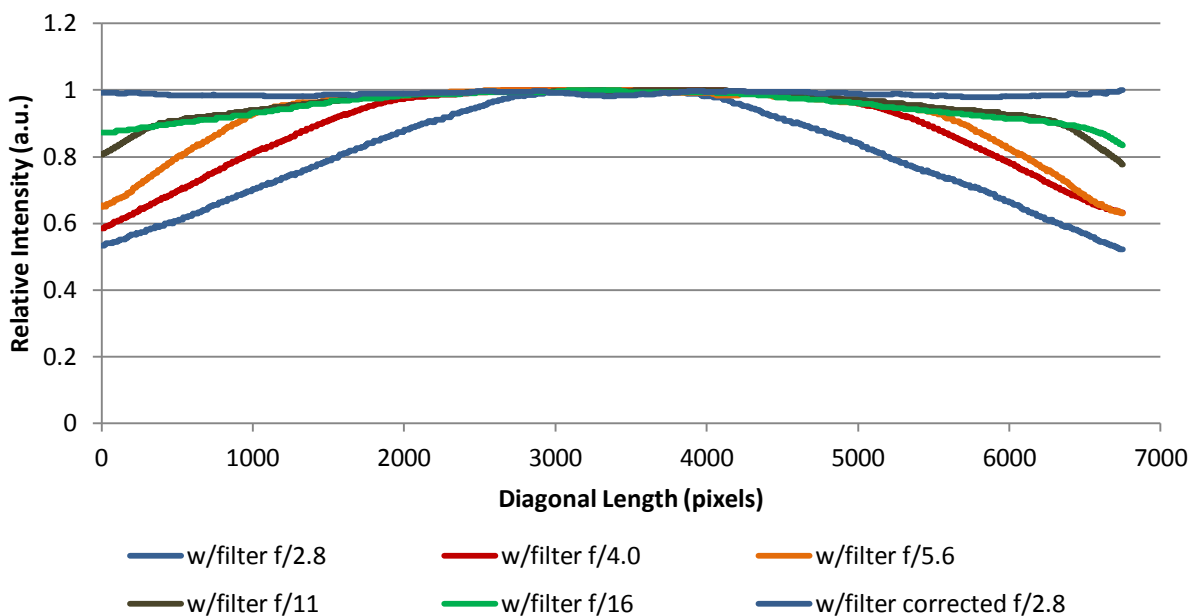


**Figure S2:** Imaging uniformity of dSLR camera using fluorescence imaging setup but with lens set at different  $f/\#$ 's or apertures. As the  $f/\#$  increases, the aperture decreases, and the exposure times required will increase linearly with the change  $f/\#$ , or 5.7x increase from  $f/2.8$  to  $f/16$ .

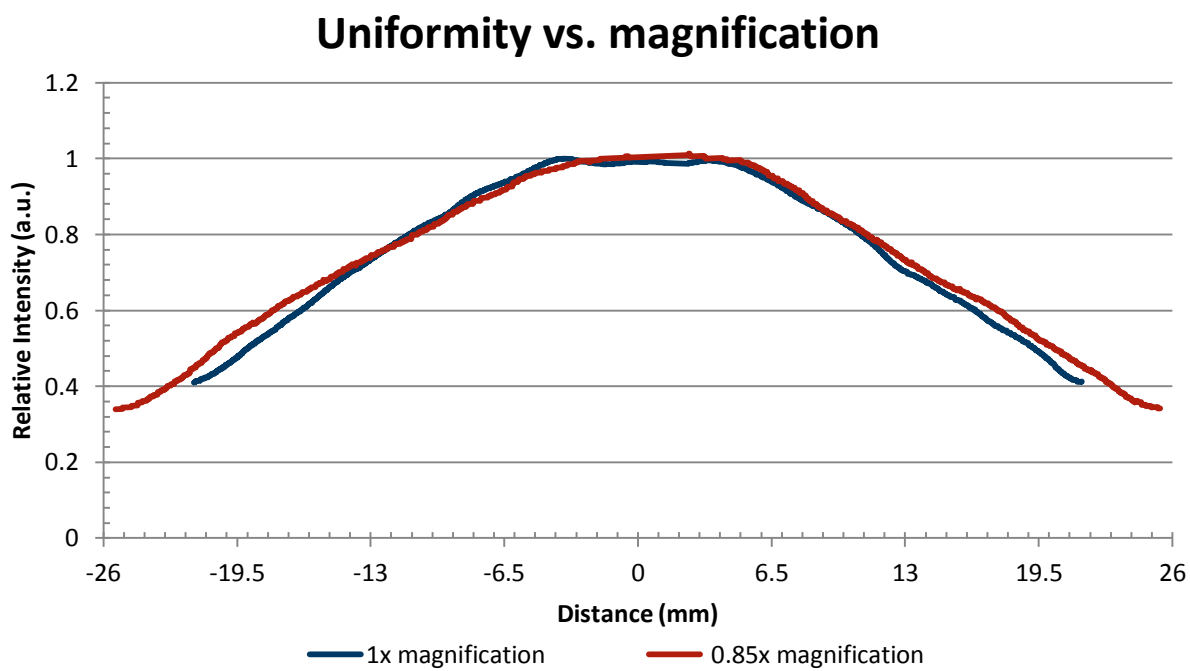


**Figure S3:** Imaging uniformity of dSLR camera using fluorescence imaging setup to compare 1x magnification uniformity with 0.85x magnification imaging uniformity at  $f/2.8$ .

## 4. Digital PCR Quantification

Digital PCR quantification proceeded with the captured image from the dSLR fluorescence imaging setup as shown in Figure 3 of the manuscript. Some variations in intensity exist over the image area resulting from different packing schemes of the droplets with higher degrees of overlap corresponding to brighter intensity areas. First, the peripheral illumination correction was performed using manufacturer-supplied software as shown in figure S4. This helped compensate for the loss in intensity at the edges resulting from the fluorescence filter. FFT analysis of a Brightfield image shows an average droplet diameter of 46  $\mu\text{m}$  and a droplet density of  $\sim 1062$  drops/ $\text{mm}^2$ . This droplet density indicates a predominately (111) packing configuration, resulting from the 66.6% w/o volume ratio used to fill the device, as apparent when looking at the lattice structure of the array. With this density, a total of  $\sim 1.1 \times 10^6$  droplets and  $\sim 55$   $\mu\text{L}$  of PCR solution are present in the 10.58  $\text{cm}^2$  droplet area. The original PCR solution was prepared with a 7,500 copies/50 $\mu\text{L}$  reaction indicating an estimated copy number 1 in  $\sim 133.3$  positive droplets on average and 8,250 total positive droplets in the entire chamber area. Correcting the chamber area to 9.6  $\text{cm}^2$  should account for  $\sim 1$ -million droplets and a 50- $\mu\text{L}$  sample volume.

The next process is completed using an imageJ or Matlab script to threshold and detect the droplets. An example script in imageJ is the following. First, the picture was cropped to the 27mm x 40.5mm chamber area containing  $\sim 1$ -million droplets, and then the black lines in the middle filled in with a background. Second, the green color channel is isolated from the red and blue channels, then an FFT bandpass filter and from 0-40 pixels was applied to the image as shown in figure S5. At this point, image processing consists of detecting regions of interest through thresholding, then quantifying the number of droplets above that threshold. Well-isolated droplets are found very quickly using a simple local maxima detection scheme. First, a threshold was defined using a maximum entropy thresholding scheme, and then local maxima detection above the threshold was used to quantify droplets of interest. Applying this simple process to Figure S5 results in a positive droplet count of  $\sim 8,058$  droplets. Alternatively, the thresholded regions can be converted to a binary image then analyzed using a built in analyze particles tool. This process simultaneously determines the shape, size, position, and other attributes from the threshold, and can also take measurements from corresponding regions of the original image. Figure S6 shows the output of the analyze particle tool after performing watershed separation techniques to separate overlapping droplets.

Experiments with higher template concentrations result in more overlapping droplets and require shape analysis and circle fitting algorithms to isolate multiple positive droplets above threshold. Using these algorithms to further process figure S5 results in an output of  $\sim 8,196$  positive droplets. This corresponds to the predicted concentration of 8,250 with less than 2% error. Adjusting the area to a smaller 9.6  $\text{cm}^2$  area results in an estimate of  $\sim 7,450$  positive droplets.

Figure S7 shows images of digital PCR DNA concentrations in 5,000, 50,000, and 100,000 copies/50 $\mu\text{l}$  rxn. From these images, it is visible that as the concentration of DNA copies increase, the ability to quantify individual droplets becomes more difficult to analyze due to such high levels of overlap and low imaging resolution.



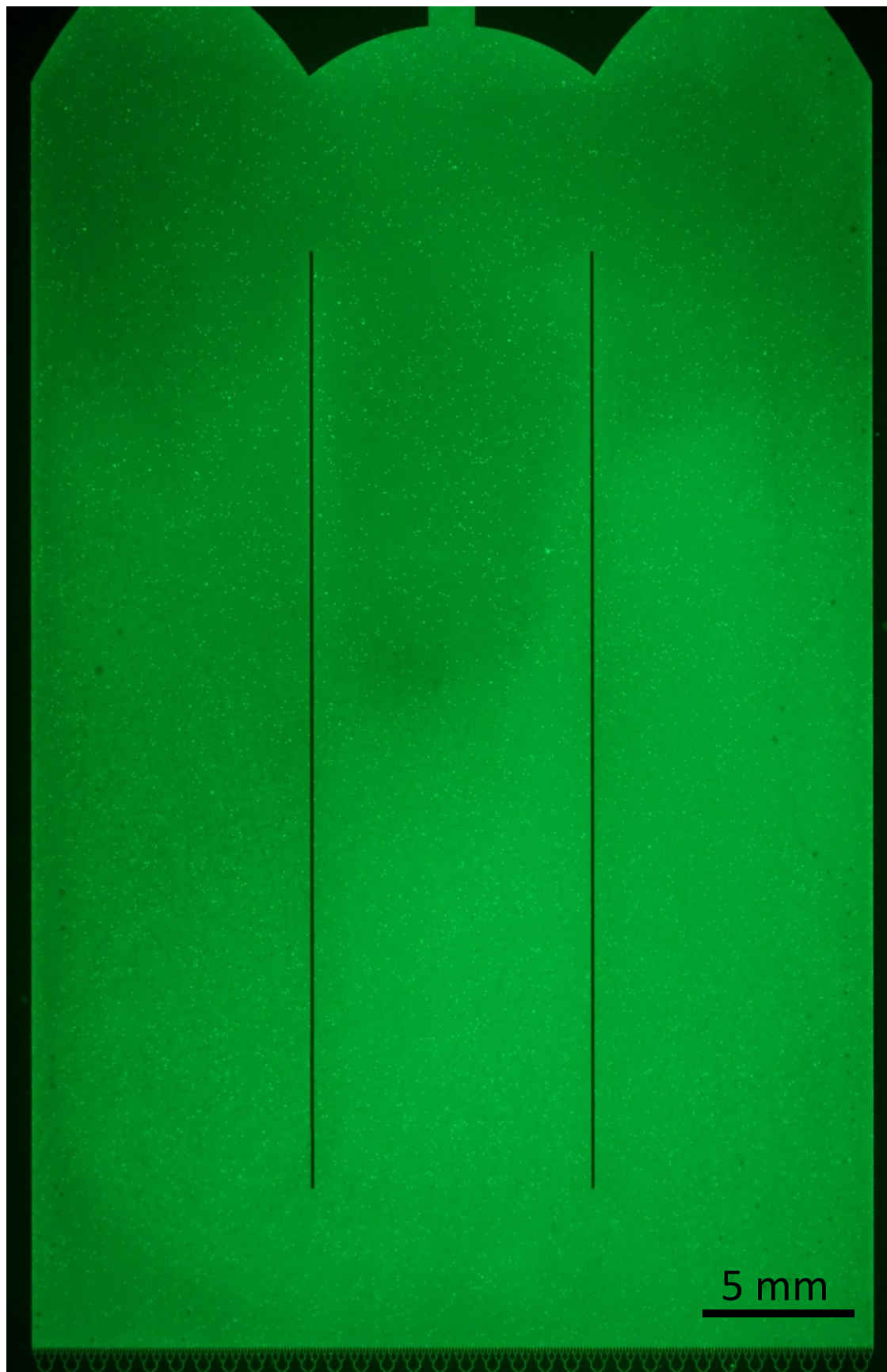


**Figure S4:** Wide-field fluorescence image of 27 mm x 40.5 mm chamber array after peripheral illumination correction. Image captured at 0.774x magnification resulting in  $\sim 8.26 \mu\text{m}/\text{pixel}$  pitch. Local variations in intensity result from differences in droplet overlap position. Brightfield image analysis



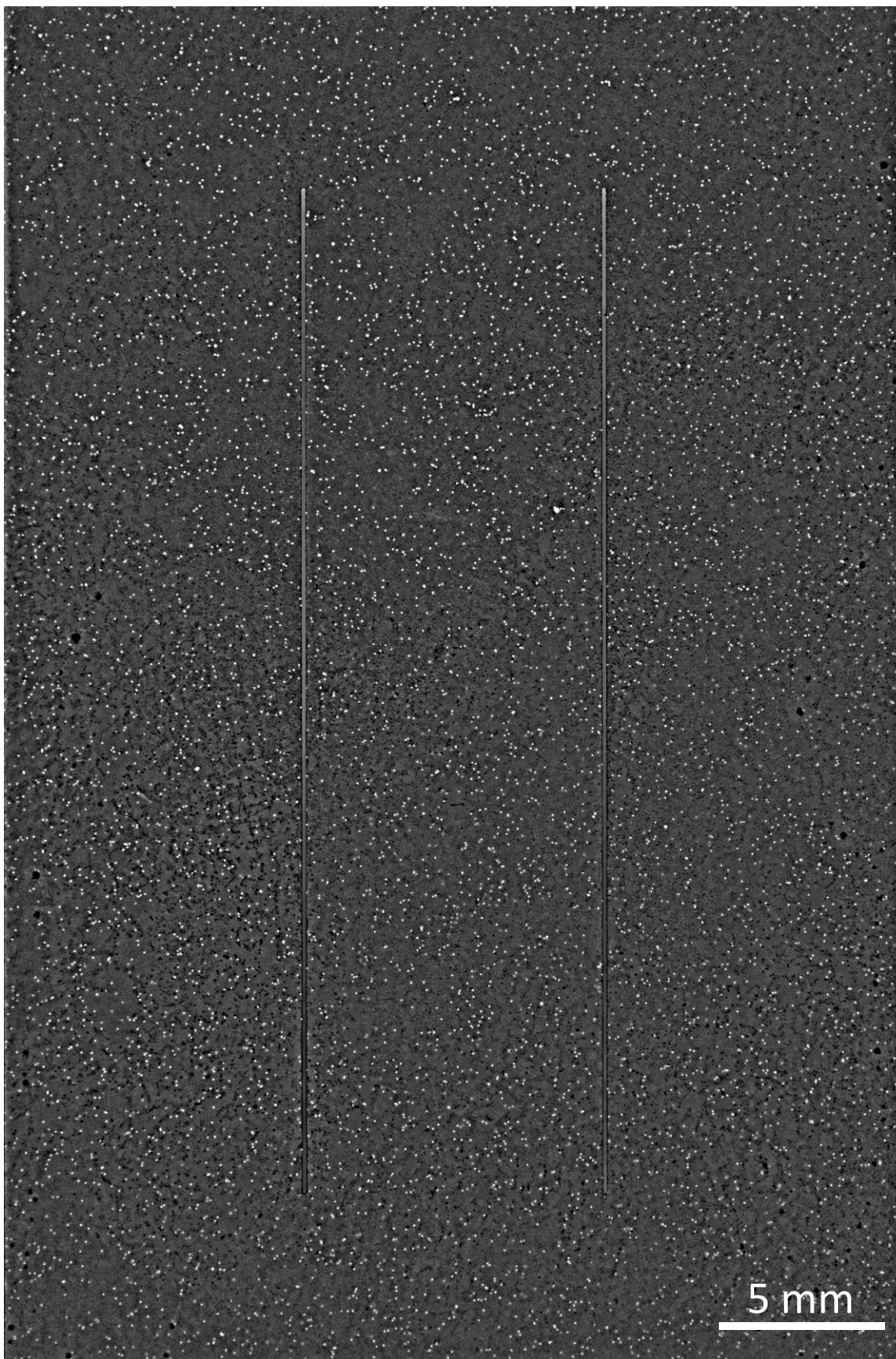


**Figure S5:** Wide-field fluorescence image of 27 mm x 40.5 mm chamber array after FFT bandpass filter of 2-40 pixels applied to image. Maximum entropy thresholding is then used to detect positive droplets from negative droplets.



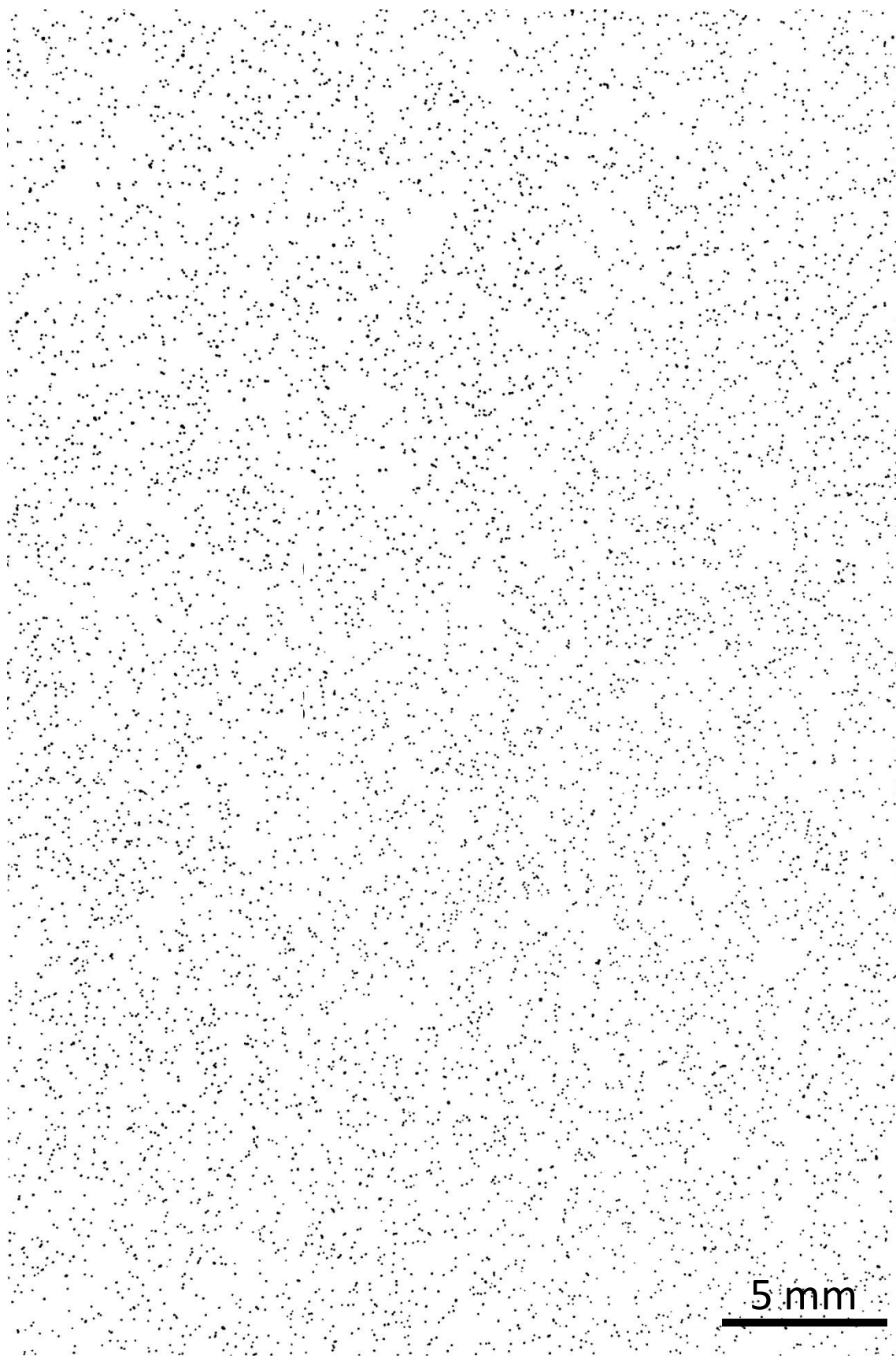


**Figure S6:** Image of mask output from analyze particle tool used to quantify and characterize the droplet array. This tool is useful to quickly analyze size, circularity, and other shape parameters to characterize results. Watershed techniques are useful to separate adjacent droplets that were connected from the thresholding output. Quantification of this image results in ~8,196 positive droplets as mentioned above.

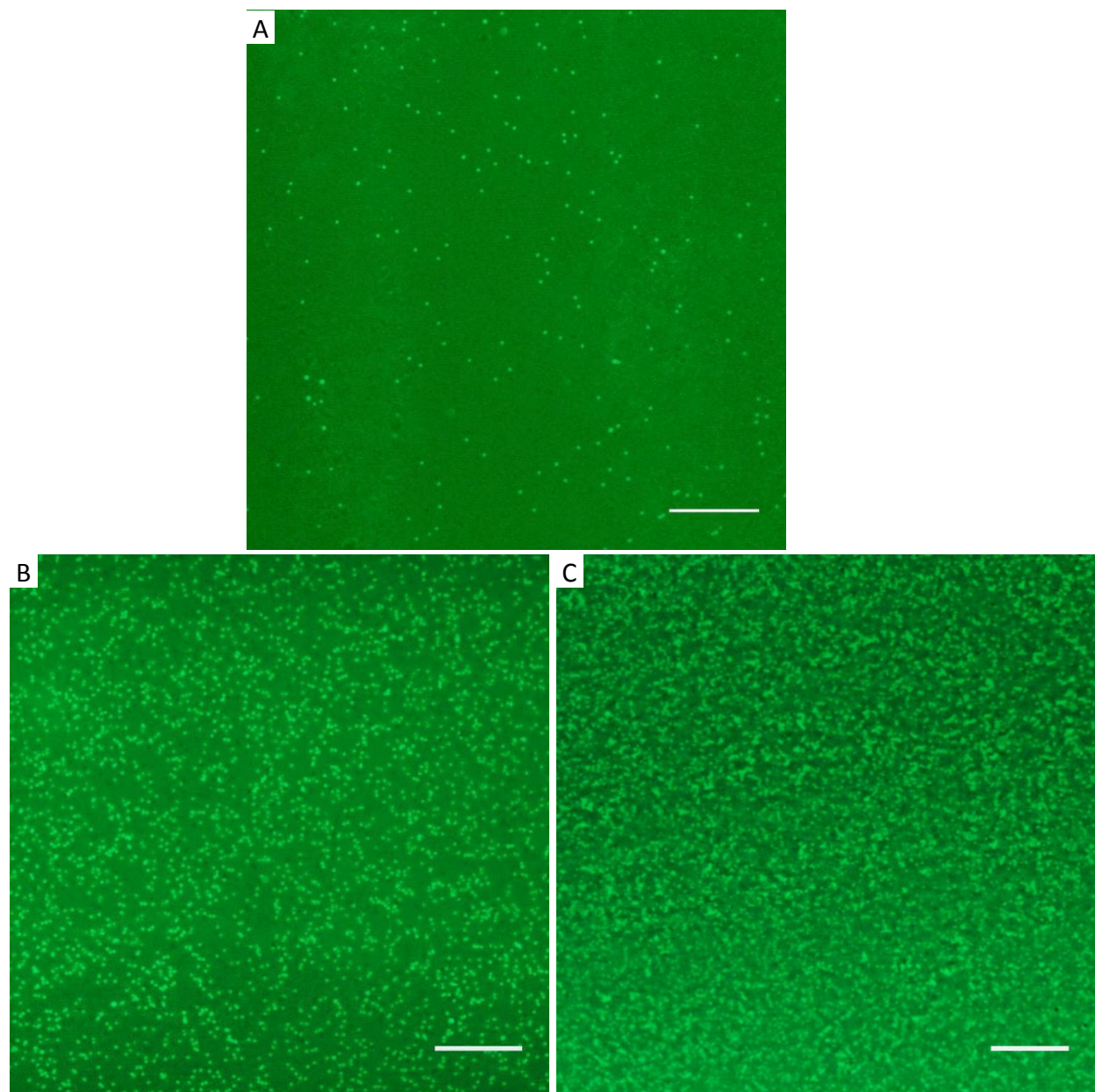
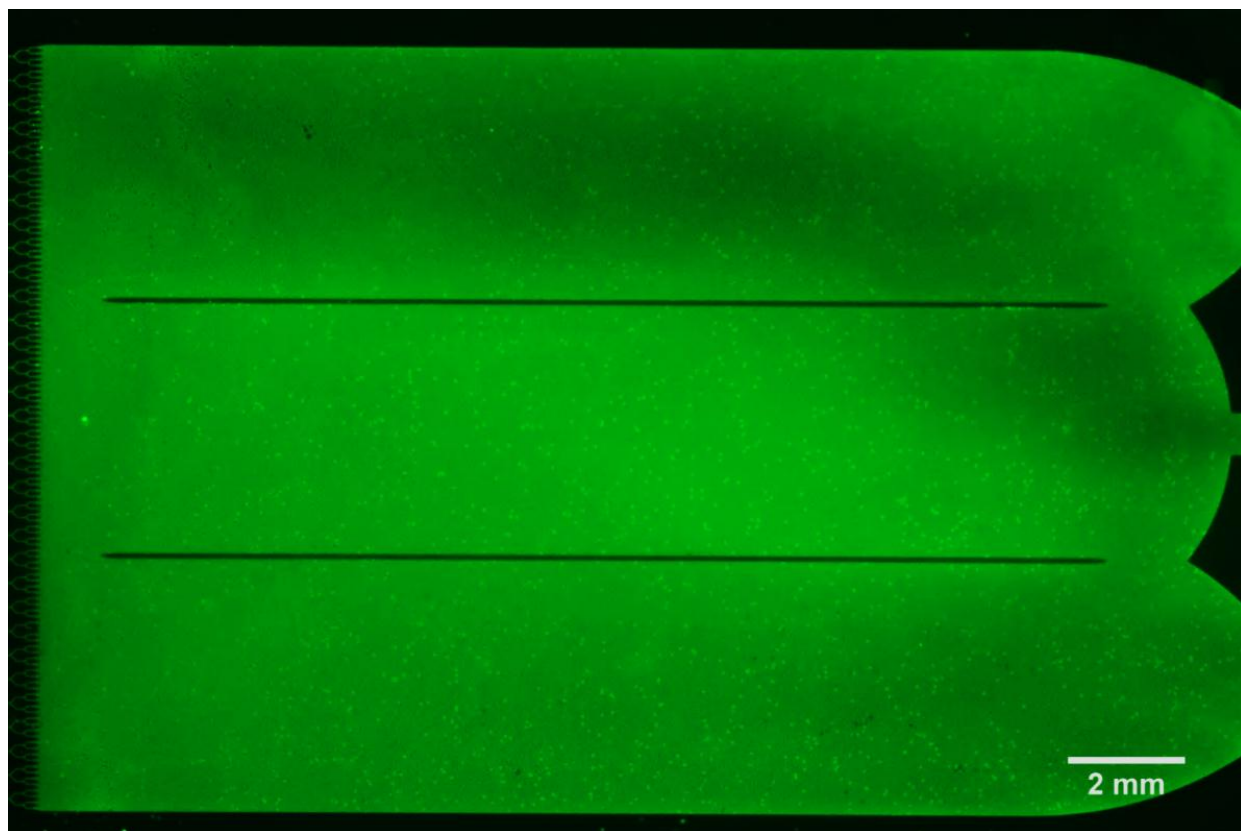


**Figure S7:** Fluorescence images of device containing A) 5,000, B) 50,000, and C) 100,000 copies / 50- $\mu$ L PCR reaction volume. Scale bars 1 mm.

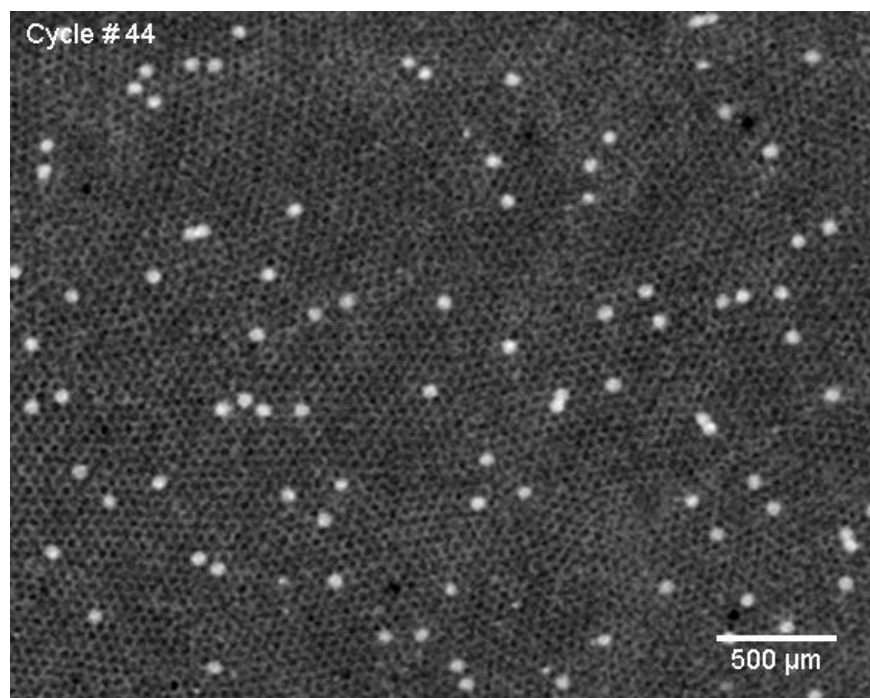
## 5. Real-Time Fluorescence Imaging

Real-time fluorescence images of PCR amplification were captured during thermocycling and assembled to create Video S2. Motion of droplets inside chamber is the result of thermal expansion and compression over successive thermocycles and an expanding air bubble trapped near the outlet. The stack of images were cropped and image registration performed using ImageJ<sup>1</sup> to create the video segment seen in Video S3. Intensity measurements of 50 positive and negative droplets are plotted in Figure S8. From this information, it is much easier to detect a positive droplet from a negative droplet because there is now both a temporal distinction as well as a fluorescence intensity distinction among droplets. This can be useful for subtracting background noise to focus only on relative changes in intensity in a droplet, and for differentiating between debris or spots that increase in intensity but are either excessively early or late relative to the PCR amplification process.



**Video S2:** Picture representing real-time PCR amplification of droplets in 4.5 cm<sup>2</sup> device at 1x magnification between cycles 15-44. The image above is an RGB 3-color image; the video shows only the green color channel.





**Video S3:** Cropped video segment of same device shown in video S1 at higher resolution. Images of each cycle were registered to align droplets from cycle to cycle.

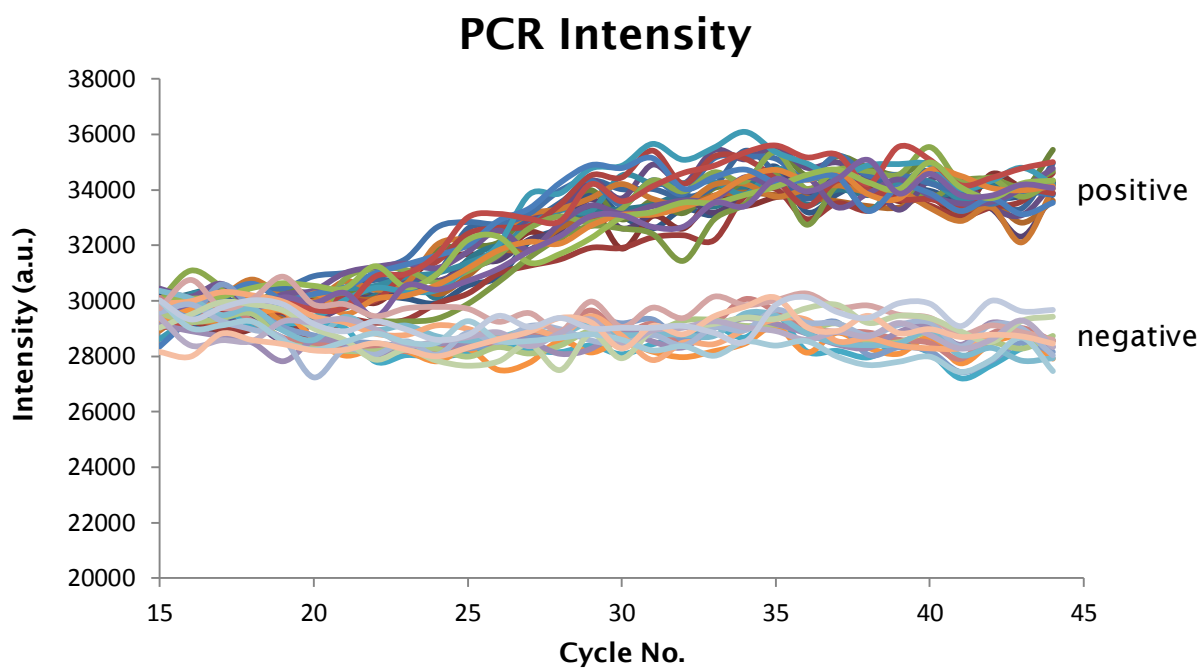


**Figure S8:** Real-time intensity measurements of PCR amplification within 50 droplets. A large amount of fluctuation in background noise occurs from cycle to cycle and is thought to be the result of droplet motion between cycles resulting in slight variations in packing formation.



## 6. Interference-Filter Behavior

Large field of view fluorescence imaging commonly involves difficulties such as achieving bright, uniform fluorescence excitation illumination and uniform image capture with low distortion. When working with large areas at close working distances, such as is common with fluorescence microscopy, light incidence angles become very large causing light intensity and uniformity to vary dramatically across the field of view. Furthermore, high quality interference filters that provide high rejection ratios and rapid wavelength cut-off transition profiles are dependent on light incidence angles. This behavior is suitable for thin collimated light paths but difficult to use in wide-field-of-view imaging setups where off-axis fluorescence signal contributions can become very large. Absorption filters are useful for absorbing light at some wavelengths but not at others, and they are very consistent over large incidence angles, but they typically suffer from slower wavelength cut-off transition profiles and are difficult to tune for the fluorophore of interest. Figure S9 shows spectrophotometer wavelength scans of the GFP-3035 interference emission filter (Semrock, USA) and two different gel absorption filters, Wratten Yellow No. 12 & 15 (Kodak, USA) at various angles of rotation using a DU 800 spectrophotometer (Beckman Coulter Inc., USA). Hybrid interference and absorption filters have been recently developed to improve filter performance in the presence of off-axis illumination, but such filters are not yet commercially available and are difficult to fabricate in house<sup>2</sup>.

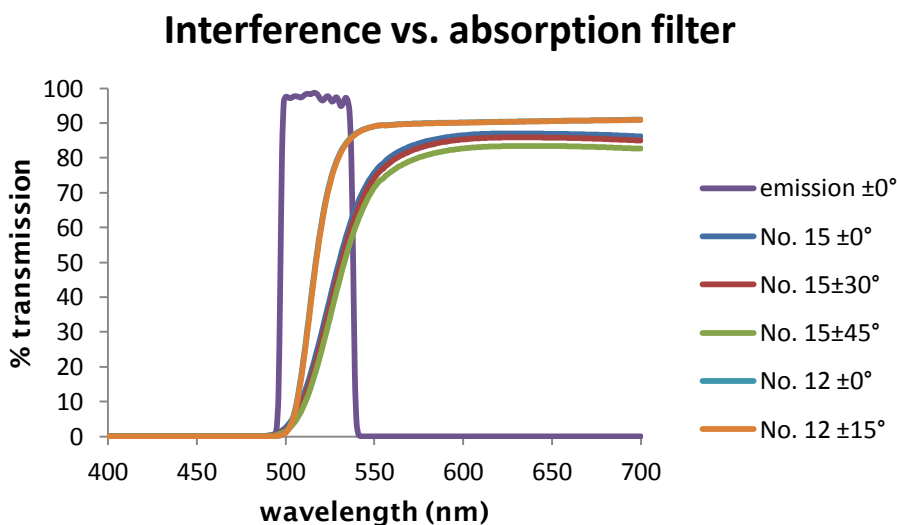


**Figure S9:** spectrophotometer wavelength scans of interference and absorption filters

More recently, lenseless wide-field fluorescence imaging approaches that use CCD or CMOS sensors for microfluidic applications have been developed that use various filtering schemes such as absorption filters combined with TIRF (total internal reflection fluorescence)<sup>3,4</sup>, and cross polarization filters<sup>5</sup>. However, these methods alone are difficult to implement with real-time PCR imaging due to thermal cycling temperatures and close coupling of the microfluidic devices with the imaging sensor. In addition, TIRF does not provide deep penetration beyond the internal reflecting surface<sup>6</sup> and would be difficult to implement with large droplet emulsions. Polarizing filters may be suitable for some wide-field imaging purposes but they are highly sensitive to auto-fluorescent materials, have poorer rejection ratios, and are sensitive to polarization shifts caused by the device or materials being imaged<sup>7</sup>.

The long working distance of the lens from the focal plane allows the placing of an interference emission filter to be placed directly in front of the camera lens and still work well. This is provided the incidence angle of light through the filter did not exceed 15° as measured on a spectrophotometer and illustrated in

Figures S10-S12. A 32mm emission filter was chosen over the standard 25mm emission filters to provide better image quality across the entire field of view as it permits more light through the 42 mm opening at the front of the Macro lens. A curve fitting of the results shown in Figure S10 shows that with increasing off-axis incidence angle,  $\theta$ , the low cutoff frequency of the filter decreases at a rate of  $494 - 0.21x - 0.02x^2$  nm. At a  $15^\circ$  off-axis incidence angle, the emission filter's low cutoff frequency was found to decrease from 494 nm to 488 nm, a difference of 6 nm.

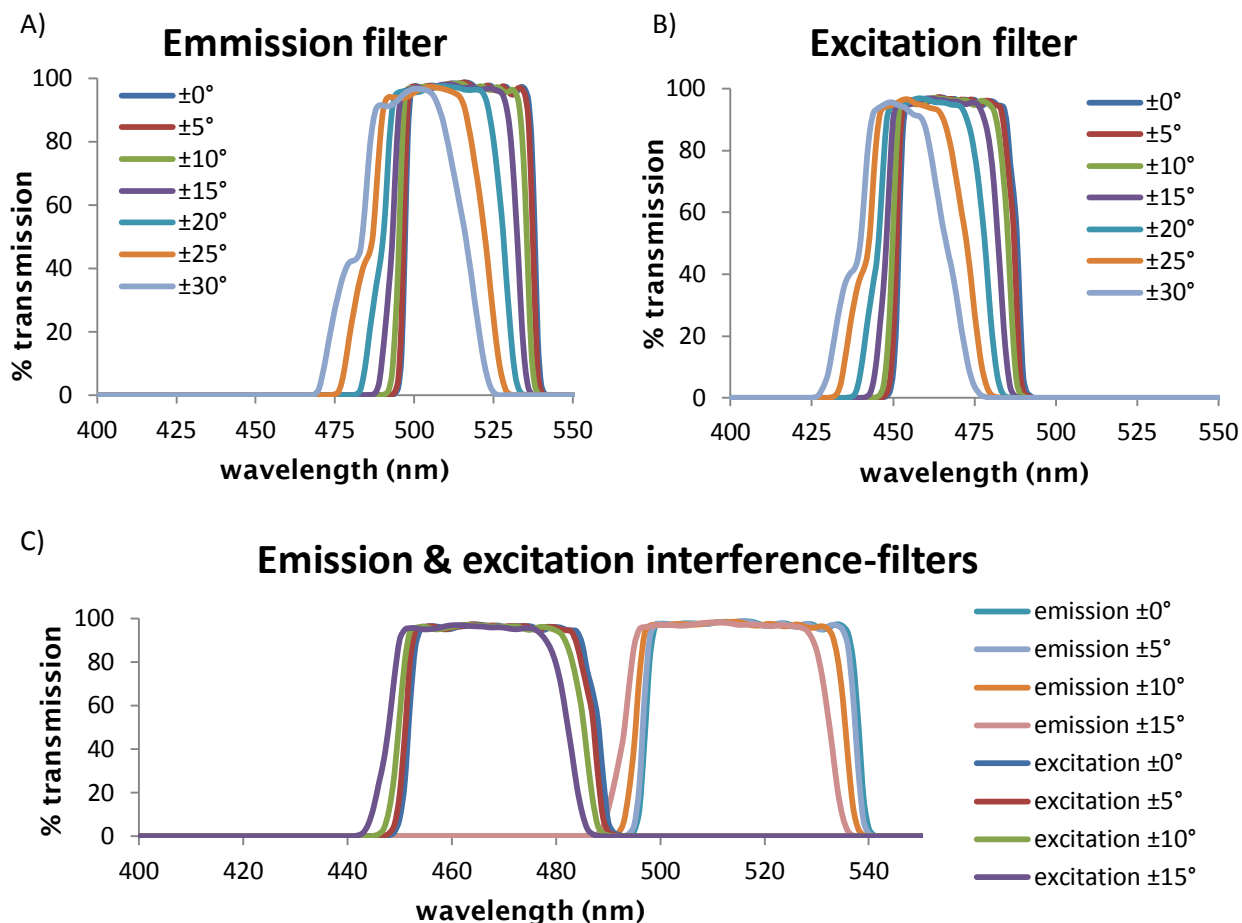


**Figure S10:** Spectrophotometer wavelength scans of interference emission and excitation filters at different angles.

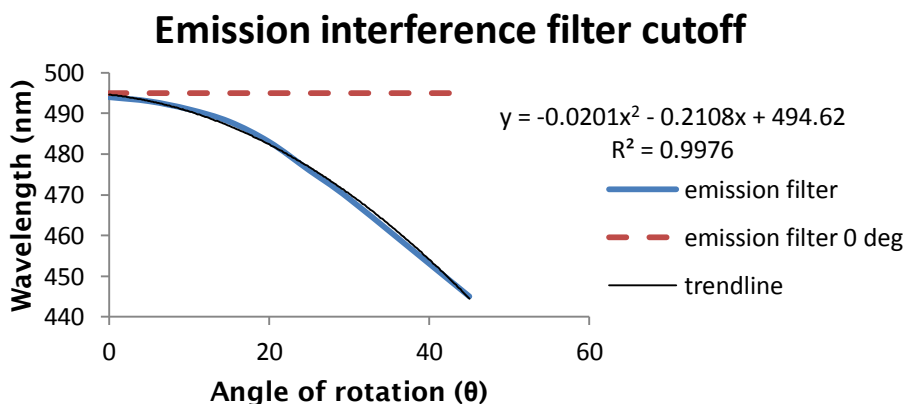


**Figure S11:** Emission filter wavelength cutoff frequency variation as a function of incidence angles

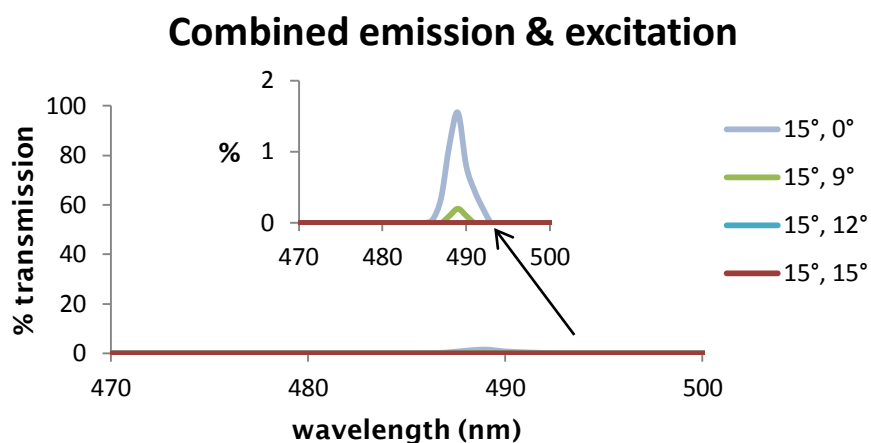


**Figure S12:** Transmission profile of light passing through first the excitation filter ( $\theta = 0\text{-}15^\circ$  variable) then emission filter ( $\theta = 15^\circ$  fixed) to illustrate improved rejection of excitation light by rotating the excitation filter and thereby shifting the excitation wavelength. Inset is a magnified view of the line graphs for visualization.

Given that the high cutoff frequency of the excitation filter is 492 nm, this allowed for some slight overlap of the two filters. This means that along the periphery of the image, where off-axis illumination is higher, the contrast ratio declines as more background excitation passes through. This slight overlap reduced the rejection ratio in the overlapping bandpass region area to less than 100:1. This problem was overcome in two ways. (1) By slightly increasing the field of view using reduced magnification, the chamber area of interest was moved closer to the image center where the angle was lower still. (2) By similarly rotating the excitation filter 10-15° relative to the excitation light source, its upper cutoff wavelength was also reduced to 488 nm, thus eliminating overlap, resulting in the original manufacturer specified rejection ratio of 1000:1. With these considerations in mind, future implementations of this imaging approach could utilize filter sets with larger separations between the emission and excitation filter cutoff wavelengths to tolerate higher incidence angles. Alternatively, the design and use of hybrid interference and absorption filter types could provide behavior that is more consistent over greater degrees of off-axis illumination<sup>2</sup>.

### References:

1. J. Greivenkamp, *Field guide to geometrical optics*, SPIE Press, Bellingham Wash., 2004.
2. W.S. Rasband, *ImageJ*, National Institutes of Health, Bethesda, MD, United States, 1997.
3. C. Richard, A. Renaudin, V. Aimez, and P. G. Charette, *Lab Chip*, 2009, **9**, 1371-1376.
4. A. F. Coskun, T.-W. Su, and A. Ozcan, *Lab Chip*, 2010, **10**, 824-827.
5. O. Mudanyali, D. Tseng, C. Oh, S. O. Isikman, I. Sencan, W. Bishara, C. Oztoprak, S. Seo, B. Khademhosseini, and A. Ozcan, *Lab on a Chip*, 2010, **10**, 1417-1428.
6. L. Shen, M. Ratterman, D. Klotzkin, and I. Papautsky, *Sensors and Actuators B: Chemical*, 2011, **155**, 430-435.
7. K. N. Fish, in *Current Protocols in Cytometry*, eds. J. P. Robinson, Z. Darzynkiewicz, J. Dobrucki, W. C. Hyun, J. P. Nolan, A. Orfao, and P. S. Rabinovitch, John Wiley & Sons, Inc., Hoboken, NJ, USA, 2009.
8. A. Pais, A. Banerjee, D. Klotzkin, and I. Papautsky, *Lab Chip*, 2008, **8**, 794-800.